

# GIR: 3D Gaussian Inverse Rendering for Relightable Scene Factorization

Yahao Shi<sup>1\*</sup> Yanmin Wu<sup>2\*</sup> Chenming Wu<sup>3#</sup> Xing Liu<sup>3</sup> Chen Zhao<sup>3</sup> Haocheng Feng<sup>3</sup>  
 Jingtuo Liu<sup>3</sup> Liangjun Zhang<sup>3</sup> Jian Zhang<sup>2†</sup> Bin Zhou<sup>1†</sup> Errui Ding<sup>3</sup> Jingdong Wang<sup>3</sup>

<sup>1</sup> Beihang University <sup>2</sup> Shenzhen Graduate School, Peking University <sup>3</sup> Baidu VIS

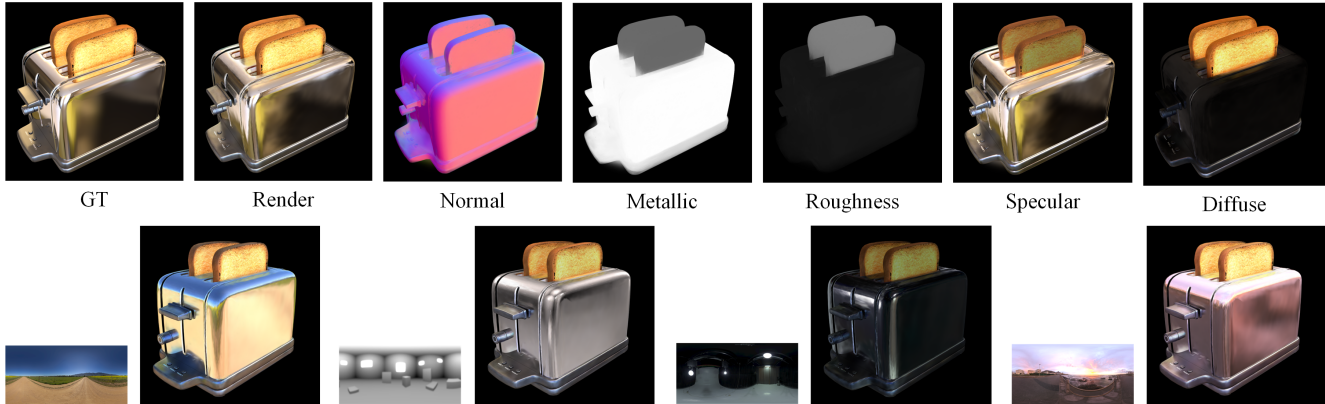


Figure 1. 3D Gaussian inverse rendering enabled by our proposed GIR. *Top*: visualization results of the factorization of geometry, spatially-varying material, and illumination, etc.. *Bottom*: relighting results under different environment maps.

## Abstract

This paper presents GIR, a 3D Gaussian Inverse Rendering method for relightable scene factorization. Compared to existing methods leveraging discrete meshes or neural implicit fields for inverse rendering, our method utilizes 3D Gaussians to estimate the material properties, illumination, and geometry of an object from multi-view images. Our study is motivated by the evidence showing that 3D Gaussian is a more promising backbone than neural fields in terms of performance, versatility, and efficiency. In this paper, we aim to answer the question: “How can 3D Gaussian be applied to improve the performance of inverse rendering?” To address the complexity of estimating normals based on discrete and often in-homogeneous distributed 3D Gaussian representations, we proposed an efficient self-regularization method that facilitates the modeling of surface normals without the need for additional supervision. To reconstruct indirect illumination, we propose an approach that simulates ray tracing. Extensive experiments demonstrate our proposed GIR’s superior performance over existing methods across multiple tasks on a variety of widely used datasets in inverse rendering. This substantiates its efficacy and broad applicability, highlight-

ing its potential as an influential tool in relighting and reconstruction. Project page: <https://3dgir.github.io>.

## 1. Introduction

Inverse rendering involves deducing scene properties from given images, including geometry, lighting, and materials. This longstanding challenge finds applications in various fields, such as scene understanding, image manipulation, AR/VR, etc. Unfortunately, inferring scene properties solely from multi-view images is an inherently ill-posed inverse problem. This is due to the intricate integral relationships defined by the rendering equation, which governs the behavior of light transport and connects geometry, materials, and illumination. Consequently, this inherent complexity gives rise to inherent ambiguities in the process.

Spatially varying material properties, illumination, and scene geometry are critical factors in determining an object’s appearance in the physical world. For example, the color of a wooden chair can change based on the type of wood; under adequate lighting, an iron teapot can reflect its surroundings with a smoothly distorted image due to its curved surface. In the early years, Nicodemus et al. [26] proposed a bidirectional reflectance distribution function (BRDF), laying the foundation for physically-based rendering by modeling the interaction of light with surfaces.

\* Equal contribution, work done while interning at Baidu VIS.

# Project lead. † Corresponding authors.

Recently, neural reconstruction methods [10, 18, 34] have demonstrated effective estimation of these factors from multi-view images using Neural Radiance Fields (NeRFs) [2, 23, 36, 39]. These methods integrate optic rendering functions that adhere to the BRDF principle into learnable neural fields, parameterized by Multilayer Perceptrons (MLPs). They estimate physically-based rendering elements, such as normals, roughness, and metallic, along with illumination and environmental maps, utilizing photometric loss calculated in the RGB color space. More recently, Kerbl et al. [14] proposed a point-based approach named 3D Gaussian Splatting (3DGS). This method represents scenes using 3D Gaussians, each defined by properties of 3D position, opacity, anisotropic covariance, and color encoded using spherical harmonic (SH) coefficients. In contrast to NeRF-based approaches, which optimize implicit representation during training, 3DGS optimizes the properties of these explicit 3D Gaussians. 3DGS has been shown as a more promising approach than NeRFs for tackling various challenges such as dynamic scene modeling [19] and content generation [33] due to its superior versatility and advanced overall performance. Furthermore, 3DGS offers real-time rendering with competitive visual quality and training efficiency compared to state-of-the-art NeRF methods, presenting an outstanding potential for a wide range of industrial and commercial usage. It is thus naturally motivated to consider: How can one achieve high-performance inverse rendering within the framework of 3DGS?

In this paper, we answer this question by introducing GIR, a novel inverse rendering framework based on 3DGS that estimates material properties, geometry, and illumination from multi-view images in high fidelity. We address the challenge of accurately modeling surface normals in 3D Gaussian representations. The complexity arises from the discrete and often in-homogeneous distribution of these Gaussians. This makes the learning of accurate normals nontrivial without the use of regularization. Moreover, the normal regularization methods designed for learning implicit Signed Distance Functions (SDF), such as the one used in [36] cannot be applied in this context. We thus propose an efficient self-regularization method that ensures the shortest axis of each visible 3D Gaussian forms an obtuse angle with the camera’s principal axis. Furthermore, we propose an approach for indirect illumination reconstruction that is suited for 3D Gaussian representation. Extensive experimental analyses have demonstrated that our proposed approach significantly outperforms existing methods on various datasets across multiple tasks. We summarize our main contributions as follows:

- We present a novel inverse rendering framework with 3DGS. This framework precisely estimates high-fidelity normal maps, specular, diffuse, roughness, metallic properties of objects, indirect illumination and environmental

maps, and supports real-time rendering.

- We propose an efficient self-regularization method that ensures the shortest axis of each visible 3D Gaussian forms an obtuse angle with the camera’s principal axis. This allows for modeling accurate normals of a surface without requiring additional supervision during training.
- Through comprehensive experimentation, we have demonstrated that our approach achieves leading performance compared to relevant schemes. The experimental results of relighting and material editing further demonstrated the superiority of the proposed framework.

## 2. Related work

### 2.1. Neural Rendering

Recent advances in neural rendering diverge into two strides, i.e., field-based neural rendering and primitive-based rendering. The most representative field-based approach is NeRF [23], which utilizes a coordinate-based MLP to encode volumetric radiance space, enabling accurate rendering of scenes. MipNeRF [2] proposes a multiscale representation for anti-aliasing, while Instant-NGP [24] combines a neural network with a multiresolution hash table for efficient evaluation. ZipNeRF [3] integrates grid-based representations and anti-aliasing for improved performance. Other approaches such as Unisurf [27], Volume [39], and NeuS [36] enhance surface reconstruction by designing proxy functions for density-to-distance field conversion, building upon NeRF’s representation.

Primitive-based rendering has a well-established history that can be traced back to earlier works such as [7, 16]. With recent neural representation advancements, NPBG [1] trains a deep rendering network to generate photorealistic images by mapping rasterized point descriptors. NPBG++ [28] improves view-dependent neural descriptors for non-Lambertian scenes without per-scene optimization. Point-NeRF [37] offers a generalizable approach using neural 3D points for scene representation and rendering. ADOP [29] utilizes a fast point cloud rasterizer with a neural network for high-quality novel view generation. Deep-Surfels [22] combines geometry and appearance using explicit and neural components. A breakthrough in 3DGS [14] introduces anisotropic 3D Gaussians and a tile-based differentiable rasterizer, advancing the field significantly. Our work embraces the principles of 3DGS while introducing the additional capability of inverse rendering for material and illumination factorization. This enhancement empowers real-time relighting and material editing, opening up new possibilities for practical applications.

### 2.2. Inverse Rendering

Given the highly underconstrained nature of the general inverse rendering problem, previous methods attempt to ad-

dress this challenge using diverse approaches. NeRV [32] assumes prior illumination knowledge and uses a computationally complex continuous volumetric function. NeRFactor [42] enhances NeRF with MLPs to describe surface properties. PhysG [41] assumes fixed illumination conditions, while NeRD [4] handles both fixed and varying illumination. Neural-PIL [5] estimates high-frequency lighting, and Ref-NeRF [34] models environment lighting and surface roughness. NVDiffrec [25] combines implicit and explicit scene representations, *i.e.*, DMTet [31]. NVDiffrecMC [10] further introduces ray tracing and Monte Carlo integration for realistic shading but exhibits unstable training performance compared to NVDiffrec [25]. Jin et al. [12] and Mai et al. [20] adopt a low-rank tensor structure for inverse rendering. NeILF [38] employs an MLP to model spatially varying illumination, capturing both direct and indirect lights. NeILF++ [40] incorporates VolSDF to learn geometry and unifies incident light and outgoing radiance through physically-based rendering. ENVIDR [17] addresses glossy surfaces, while NeRO [18] focuses on reconstructing reflective objects, and similar approaches are also drawn in [9, 21]. Building upon remarkable designs from prior literature, our work exhibits exceptional capabilities by enabling seamless end-to-end training and inference without the need for mesh conversion. Naturally, it enables real-time rendering and material editing, distinguishing it as a significant contribution to the field.

### 3. Method

In this section, we present our 3D Gaussian inverse rendering framework, which enables geometry, illumination, material factorization, and real-time relighting. It processes a collection of posed images and outputs optimized 3D Gaussians, detailing densities, normals, material properties, and an image-based environment map. We apply physically-based light transport to 3DGS to render the scene’s appearance (Sec. 3.1). To successfully achieve the goal of relightable scene factorization, we introduce a series of modules, including normal estimation (Sec. 3.2) for constructing a plausible representation of normal, intrinsic image decomposition (Sec. 3.3), indirect illumination for modeling the inter-bounce within the target scene (Sec. 3.4), and loss function optimization (Sec. 3.5).

#### 3.1. Rendering

**Gaussian Splatting.** 3DGS proposes a fast alpha-blending technique for neural rendering without deep networks. This is achieved by optimizing a differentiable scene representation that can be easily projected to 2D splats. 3D Gaussians are typically based on sparse Structures from Motion (SfM) points without normals. They are defined by a full 3D covariance matrix  $\Sigma$ , established in world space and centered

at the point  $\mathbf{x}$  with spatial mean  $\mu$  and covariance matrix  $\Sigma$ :

$$G(\mathbf{x}) = e^{-\frac{1}{2}(\mathbf{x}-\mu)^\top \Sigma^{-1}(\mathbf{x}-\mu)}. \quad (1)$$

To simplify the process of obtaining the covariance matrix  $\Sigma$ , 3DGS offers a more intuitive yet equally expressive representation by describing the configuration of an ellipsoid, which includes a scaling matrix  $S$  and a rotation matrix  $R$ . Consequently, the covariance matrix can be decomposed into two components:

$$\Sigma = R S S^\top R^\top. \quad (2)$$

By applying alpha-blending to the  $N$  sorted Gaussians for each screen pixel, we can compute its color  $C$  based on the overlapping points as follows:

$$C = \sum_{i \in N} T_i \alpha_i c_i, \quad (3)$$

where  $T_i = \prod_{j=1}^{i-1} (1 - \alpha_j)$  represents the transmission of the  $i$ -th sorted Gaussian. The variable  $c_i$  represents the color of each Gaussian, and  $\alpha_i$  is computed based on the per-point opacity by multiplying the deviator component of the covariance matrix  $\Sigma$  projected onto the 2D screen.

**BRDF Rendering.** To enable the physically-based rendering of 3D Gaussians, we parametrize each Gaussian by an additional set of terms to optimize, *i.e.*, normal  $\mathbf{n} \in \mathbb{R}^3$ , roughness  $r \in [0, 1]$ , and metallic  $m \in [0, 1]$ . The rendering equation involves the calculation of the outgoing light from a Gaussian with point  $\mathbf{x}$  based on the given BRDF properties, it relates the incident light to the Gaussian with the outgoing light.

$$L_o(\omega_o, \mathbf{x}) = \int_{\Omega} f(\omega_o, \omega_i, \mathbf{x}) L_i(\omega_i, \mathbf{x}) (\omega_i \cdot \mathbf{n}) d\omega_i, \quad (4)$$

where the viewing direction of the outgoing light is represented by  $\omega_o$ ,  $L_i$  corresponds to the incident light coming from direction  $\omega_i$ , and  $f$  represents the BRDF properties of the point. The integration domain is the upper hemisphere  $\Omega$  defined by the point  $\mathbf{x}$  and its normal  $\mathbf{n}$ . The BRDF property  $f$  can be divided to diffuse and specular components according to the Disney BRDF model [6] as follows.

$$f(\omega_o, \omega_i) = (1 - m) \frac{\mathbf{a}}{\pi} + \frac{DFG}{4(\omega_i \cdot \mathbf{n})(\omega_o \cdot \mathbf{n})}, \quad (5)$$

where  $\mathbf{a}$  is the first order of color  $c$  of the Gaussian, which represents the base color.  $D$  is the normal distribution function,  $F$  is the Fresnel term and  $G$  is the geometry term. The detailed computations of  $D$ ,  $F$ ,  $G$  are related to roughness  $r$  and metallic  $m$ , which can be referred to [35].

In order to simplify the computation involved in 3DGS, we employ the *split-sum* approximation [13], which has been proved effective in many industrial applications and previous works [18, 21, 25]. This approximation allows us to separate the integral of the product of lights and BRDFs into two separate integrals, each of which can be pre-calculated and stored for efficient querying. Specifically, the specular term can be approximated by:

$$c_{\text{specular}} \approx I(\mathbf{r}, r) \cdot \int_{\Omega} \frac{DFG}{4(\boldsymbol{\omega}_o \cdot \mathbf{n})} d\boldsymbol{\omega}_i, \quad (6)$$

where  $I$  involves an important sampling of incident light radiance mediated by the reflection direction  $\mathbf{r} = 2(\boldsymbol{\omega}_i \cdot \mathbf{n})\mathbf{n} - \boldsymbol{\omega}_i$  and roughness  $r$ . This can be approximated by further assuming the viewing angle is aligned with the normal, *i.e.*,  $\mathbf{n} = \boldsymbol{\omega}_o$ , such that

$$I(\mathbf{r}, r) = \int_{\Omega} L_i(\boldsymbol{\omega}_i) D(\boldsymbol{\omega}_i, \mathbf{n}; r) (\boldsymbol{\omega}_i \cdot \mathbf{n}) d\boldsymbol{\omega}_i. \quad (7)$$

The remaining part of Equ. 6 can be pre-computed exactly since it is independent of illumination and represents the integration of specular BRDF in a constant white environment. With the help of Schlick’s equation [30], we can factorize the specular reflectance  $F_0$  at normal incidence. Consequently, this can be expressed as the modulation of  $F_0$  by its scale and bias which is solely dependent on the material’s roughness and the cosine between the viewing angle and the surface normal vector ( $\mathbf{v} \cdot \mathbf{n}$ ). The scale and bias can be precomputed and stored as a 2D look-up table (LUT) for optimizing inference efficiency. In accordance with the convention established in [13], we define  $F_0$  as an interpolated value between 0.04 (representing the specular reflectance of non-metallic materials) and the albedo  $\mathbf{a}$ , taking into account the material’s metallic value  $m$ .

$$F_0 = 0.04 \times (1 - m) + m\mathbf{a}. \quad (8)$$

The diffuse color can be written as

$$c_{\text{diffuse}} = \mathbf{a}(1 - m) \int_{\Omega} L(\boldsymbol{\omega}_i) \frac{\boldsymbol{\omega}_i \cdot \mathbf{n}}{\pi} d\boldsymbol{\omega}_i, \quad (9)$$

where the integral term can be efficiently calculated from the mipmap image-based light. Based on all the computations above, we can obtain the final color  $c_{\text{final}} = c_{\text{diffuse}} + c_{\text{specular}}$ .

**Light Representation.** As there exist multiple bounces in between Gaussians, to tackle the difficulty in simulating indirect illumination, we propose to model the indirect illumination using an approximate approach as explained in Sec. 3.4. This results in separately modeling the light as direct light  $L_{\text{dir}}$  and indirect light  $L_{\text{ind}}$ . In particular, the incident illumination is modeled by

$$L_i(\boldsymbol{\omega}_i, \mathbf{x}) = V(\boldsymbol{\omega}_i, \mathbf{x}) L_{\text{dir}}(\boldsymbol{\omega}_i) + L_{\text{ind}}(\boldsymbol{\omega}_i, \mathbf{x}), \quad (10)$$

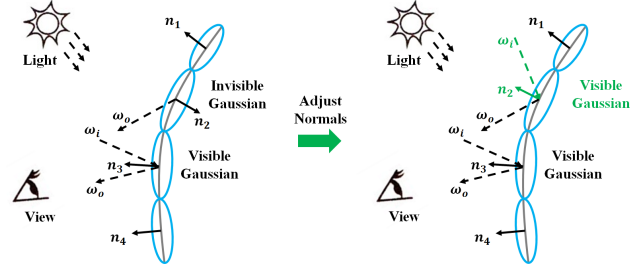


Figure 2. Gaussians present on the surface and observed from the viewpoint should be visible. Any Gaussian that is not visible, as determined by  $\mathbf{n} \cdot \mathbf{v} \leq 0$ , does not contribute to color calculations. Therefore, the normal direction of these invisible Gaussians needs to be modified in order to reconstruct the desired image.

where  $V(\boldsymbol{\omega}_i, \mathbf{x})$  represents light visibility from the outside of the bounding sphere of the scene. The direct light contributes a significant part to the rendering of the scene, and it can be efficiently computed by splitting the sum into two integrals. We use image-based light representation to model the direct light  $L_{\text{dir}}$ , which can be efficiently pre-integrated using mipmap stored at different roughness scales. As stated in Sec. 3.4, we use SH coefficients to represent the indirect light  $L_{\text{ind}}$ , and apply a similar approximation method in [18] to avoid multiple evaluations.

### 3.2. Normal Estimation

Our inverse rendering method leverages the advanced 3DGS technique for 3D geometry representations. However, the standard 3DGS approach does not simultaneously optimize the point normal  $\mathbf{n}$ . Estimating normals from discrete entity points is challenging, as all 3D Gaussians are optimized independently. Previous works often compute normals by relying on a continuous surface, such as a mesh and an SDF. In our exploration of 3DGS, we made an interesting observation: the maximum cross-section of an ellipsoid, oriented towards a specific angle, contributes the most to the visible views in neural rendering. Therefore, we intuitively and innovatively adopt the shortest axis of an ellipsoid to represent the point normal.

Put simply, we can compute the eigenvalues and eigenvectors for the positive definite matrix  $\Sigma$  using spectral decomposition for each 3D Gaussian. Subsequently, we consider the eigenvector associated with the smallest eigenvalue as the point normal. In a more simplified manner, we found that the eigenvalues are  $S^2$  according to Equ. 2. Hence, we select the shortest rotation matrix  $R$  axis to approximate the point normal  $\mathbf{n}$ . It is important to note that the smallest eigenvector and the actual point normal are often not in the same direction and can even be opposite. This discrepancy arises because when splatting Gaussians onto 2D screen pixels, there is no need to distinguish between an ellipsoid’s positive and negative sides. Therefore, to opti-

mize the normal  $\mathbf{n}$  associated with the rotation matrix  $R$ , it is necessary to specify the orientation for each Gaussian.

In 3DGS, the SH coefficients are optimized to capture the view-dependent appearance of 3D models. However, in our implementation, we use the albedo color  $c \in \mathbb{R}^3$  for each Gaussian. This is because the albedo color of each Gaussian should appear the same in all views, and the view-dependent appearance is primarily determined by the viewpoints  $o$ . To determine the visibility of a point, we compute the dot product between the normal  $\mathbf{n}$  and the view direction  $\mathbf{v} = o - \mu$ , where  $\mu$  represents the mean position of the Gaussian. We can define visible and invisible points based on the value of  $\mathbf{n} \cdot \mathbf{v}$ , and obtain a boolean visible mask as follows:

$$M = \begin{cases} 0, & \mathbf{n} \cdot \mathbf{v} \leq 0, \\ 1, & \mathbf{n} \cdot \mathbf{v} > 0. \end{cases} \quad (11)$$

We can then modify the alpha-blending function (Equ. 3) to incorporate the visible mask  $M$ :

$$C = \sum_{i \in N} T_i M_i \alpha_i c_i. \quad (12)$$

The function defines that points containing back-view normals (where  $\mathbf{n} \cdot \mathbf{v} \leq 0$ ) will not contribute to the calculation of colors. In the normal estimation, as illustrated in Fig. 2, points on the visible surface will have their normals adjusted to reconstruct the desired image, while points on the invisible surface will not be affected, as the alpha-blending process concludes for those points. This operation allows us to obtain a sufficiently accurate normal for each Gaussian, which can be used in subsequent steps of the rendering process.

Indeed, our normal estimation method fully utilizes the properties of Gaussians without introducing additional parameters, and it has been proven to work well. This approach helps maintain the simplicity of the Gaussian representation and rendering formulations while effectively estimating surface normals. Moreover, the supervision for normal estimation only relies on color reconstruction, which is self-supervised without explicit regularization and loss. This self-supervised nature simplifies the training process and reduces the need for additional annotations or complex loss function design.

### 3.3. Intrinsic Image Decomposition

To decompose the intrinsic image for inverse rendering, we adopt physically-based rendering to achieve the BRDF rendering, as discussed in Section 3.1. As we have introduced two additional trainable variables for physically-based rendering, namely the metallic parameter  $m$  and the roughness parameter  $r$ , for each Gaussian, the splatting equation (Equ. 3) can be rewritten as follows:

$$C = \sum_{i \in N} T_i M_i \alpha_i \hat{c}_i, \quad (13)$$

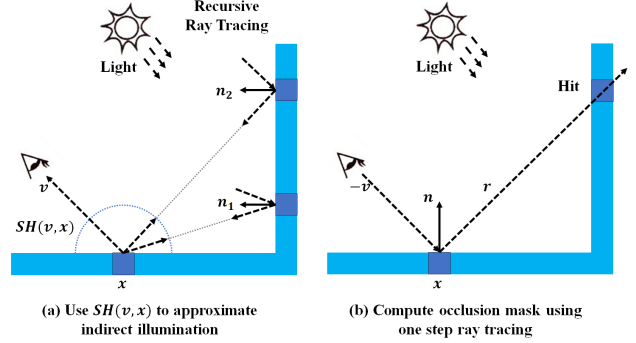


Figure 3. The illustration of our indirect illumination reconstruction: (a) Instead of employing recursive ray tracing, we utilize spherical harmonic coefficients to encode the view direction, enabling the simulation of indirect illumination. (b)

where  $\hat{c}_i = l_s(c_i, m, r, \mathbf{n}, \mathbf{v}) + l_d(c_i, m, \mathbf{n})$ . *i.e.*, we replace the albedo color  $c$  with color  $\hat{c}$  after physically-based rendering for each Gaussian. Here,  $l_s$  and  $l_d$  are two functions used for computing specular and diffuse color, respectively, according to Equ. 6 and Equ. 9.

To obtain the diffuse component and specular component of illumination, we introduce a differentiable function  $g_\theta : \mathbb{R}^{64 \times 128} \rightarrow \mathbb{R}^{1024 \times 2048}$  to generate and optimize environment light maps  $l$ . We then convert the environment light into cube maps and utilize the mipmaps for the physically-based rendering pipeline. In our implementation,  $g_\theta$  starts with a learnable constant and is a Fully Convolutional Network (FCN) with up-sample layers. The FCN consists of convolution layers with LeakyReLU activation functions. After two convolution layers, the feature map resolution is doubled. The trainable variables  $\theta$  are optimized during training, resulting in high-fidelity and smooth environment light maps.

### 3.4. Indirect Illumination

Indirect illumination is commonly present in objects that experience self-occlusion. However, it poses a challenge to model indirect illumination in 3DGS appropriately. Generally, recovering indirect illumination involves recursive path tracing based on a continuous surface such as a mesh, making inverse rendering computationally intractable. This paper presents an approximate ray tracing approach to simulating spatially varying indirect illumination from Gaussians. Our key insight is to decompose indirect illumination into two components: SH coefficients represented as colors and a view-dependent occlusion mask that determines the visibility of indirect illumination, as illustrated in Fig. 3.

The indirect incoming light  $L_{\text{ind}}(\mathbf{v}, \mathbf{x})$  at position  $\mathbf{x}$  is obtained by sampling and integrating rays over the hemisphere following ray tracing. However, as the number of considered bounces increases, the computation for tracing

and rendering grows exponentially with the sample amount. To tackle this issue, we utilize trainable SH coefficients by encoding the view direction  $\mathbf{v}$  to simulate the integrated color at point  $\mathbf{x}$ . This approach allows us to approximate the indirect illumination while reducing the computational complexity compared to traditional ray tracing methods.

According to the light representation (Equ. 10), we utilize an occlusion mask  $M_{\text{occ}}$  that is predicted through a one-step ray tracing process to determine whether indirect lights will be used in rendering. The ray originating from point  $\mathbf{x}$  and directed towards the reflection direction  $\mathbf{r}$  is occluded by surfaces within the bounding sphere. Then, we consider that point  $\mathbf{x}$  in the direction  $\mathbf{r}$  has an occlusion mask. Since the geometry is fixed, we directly compute the occlusion mask by tracing rays within the given geometry rather than predicting it using additional trainable parameters. Thus, the light combined with direct illumination and indirect illumination is as follows:

$$L(\mathbf{v}, \mathbf{x}) = (1 - M_{\text{occ}}) * L_{\text{dir}}(\mathbf{v}) + L_{\text{ind}}(\mathbf{v}, \mathbf{x}). \quad (14)$$

To efficiently obtain an occlusion mask  $M_{\text{occ}}$  based on Gaussians at a specific view, we first convert the Gaussians into binary (0/1) grids to simulate the surface. Each Gaussian will have a reflection direction  $\mathbf{r}$  that depends on the point normal  $\mathbf{n}$  and the view direction  $\mathbf{v}$ . Then, we sample points on the reflection direction within a specific length and query whether the reflection direction intersects with the grid.

### 3.5. Joint Optimization

To optimize our method, we introduce regularization for color, depth, normal, metallic, roughness, and environmental light. Moreover, we slightly scale the maximum value of  $S$  to improve performance. The image reconstruction loss function combines Mean Absolute Error (MAE) denoted as  $\mathcal{L}_{\text{MAE}}$  with a D-SSIM term denoted as  $\mathcal{L}_{\text{SSIM}}$ . This combined loss function allows for a comprehensive evaluation of the image reconstruction process, considering the absolute differences and the structural similarities between the generated image and the ground truth.

To achieve smooth features on a pixel level,  $\mathcal{L}_{\text{smooth}}(x)$  represents a spatial smoothness term that penalizes the L1 norm of second-order gradients of features along both the  $x$  and  $y$  directions. This encourages depth, normal, metallic, and roughness values to align on planar surfaces when no image gradient appears. The formulation of  $\mathcal{L}_{\text{smooth}}(x)$  is as follows:

$$\mathcal{L}_{\text{smooth}}(x) = \sum_p \sum_{d \in \{x, y\}} |\nabla_d^2 x(p)| e^{\nabla_d I(p)}, \quad (15)$$

where  $p$  represents the location of each pixel, and  $I$  is the ground truth image. This term introduces a smooth

constraint on depth  $\mathcal{L}_{\text{smooth}}(d)$ , normal  $\mathcal{L}_{\text{smooth}}(n)$ , metallic  $\mathcal{L}_{\text{smooth}}(m)$ , and roughness  $\mathcal{L}_{\text{smooth}}(r)$  respectively, helping to ensure that these properties exhibit smooth variations across the surface.

The light regularization  $\mathcal{L}_{\text{light}}$  [38] is designed to ensure that the lighting is neutral and white. This is achieved by computing the mean of the cube maps of the environment light and minimizing the difference between the RGB values and their mean using the following equation:

$$\mathcal{L}_{\text{light}} = \sum_{i=1}^3 (l_i - \sum_{j=1}^3 l_j), \quad (16)$$

where  $l_i$  and  $l_j$  represent the individual RGB components of the light. Therefore, the final optimization loss function with coefficients  $\{\lambda_i | i = 1, 2, \dots, 6\}$  are as follows:

$$\begin{aligned} \mathcal{L} = & (1 - \lambda_1) \mathcal{L}_{\text{MAE}} + \lambda_1 \mathcal{L}_{\text{SSIM}} + \lambda_2 \mathcal{L}_{\text{smooth}}(d) + \\ & \lambda_3 \mathcal{L}_{\text{smooth}}(n) + \lambda_4 \mathcal{L}_{\text{smooth}}(m) + \lambda_5 \mathcal{L}_{\text{smooth}}(r) + \lambda_6 \mathcal{L}_{\text{light}} \end{aligned} \quad (17)$$

## 4. Experiments

### 4.1. Implementation and Baselines

We implement the proposed GIR framework using Pytorch and CUDA, and conduct all the experiments on a single NVIDIA V100 GPU with 32GB VRAM. We train GIR on each object for 30k steps overall and use a batch size of 1 image per iteration with the Adam optimizer [15] ( $\beta_1 = 0.9$ ,  $\beta_2 = 0.999$ ), which accounts for 8–9 GB VRAM usage. The learning rates and schedules for the most trainable parameters are identical to the settings in 3DGS. Besides, we set learning rates for the additional parameters. *i.e.*, the learning rate for metallic and roughness are four times that for environment light, starting at 0.001 and decreasing to 0.0001 after 30k steps.

For the baselines, we consider methods that are capable of reconstructing all three scene properties, including surface geometry, materials, and illumination. Specifically, we select a variety of related approaches, NeRFactor [42], NVDiffRec [25], NVDiffrecMC [11], Factored-NeuS[9], ENVIDR [17], InvRender [44], and TensorIR [12] as our main competitors, taking into account their popularity and the availability of their source code. The technical contributions of these approaches are summarized in Sec. 2.

### 4.2. Metric

To assess the quality of rendering, materials, and illumination, we use the Peak Signal-to-Noise Ratio (PSNR) metric, where higher values indicate better quality. Following the method of InvRender [44], we incorporate masks to compute the PSNR specifically in the foreground. This enables

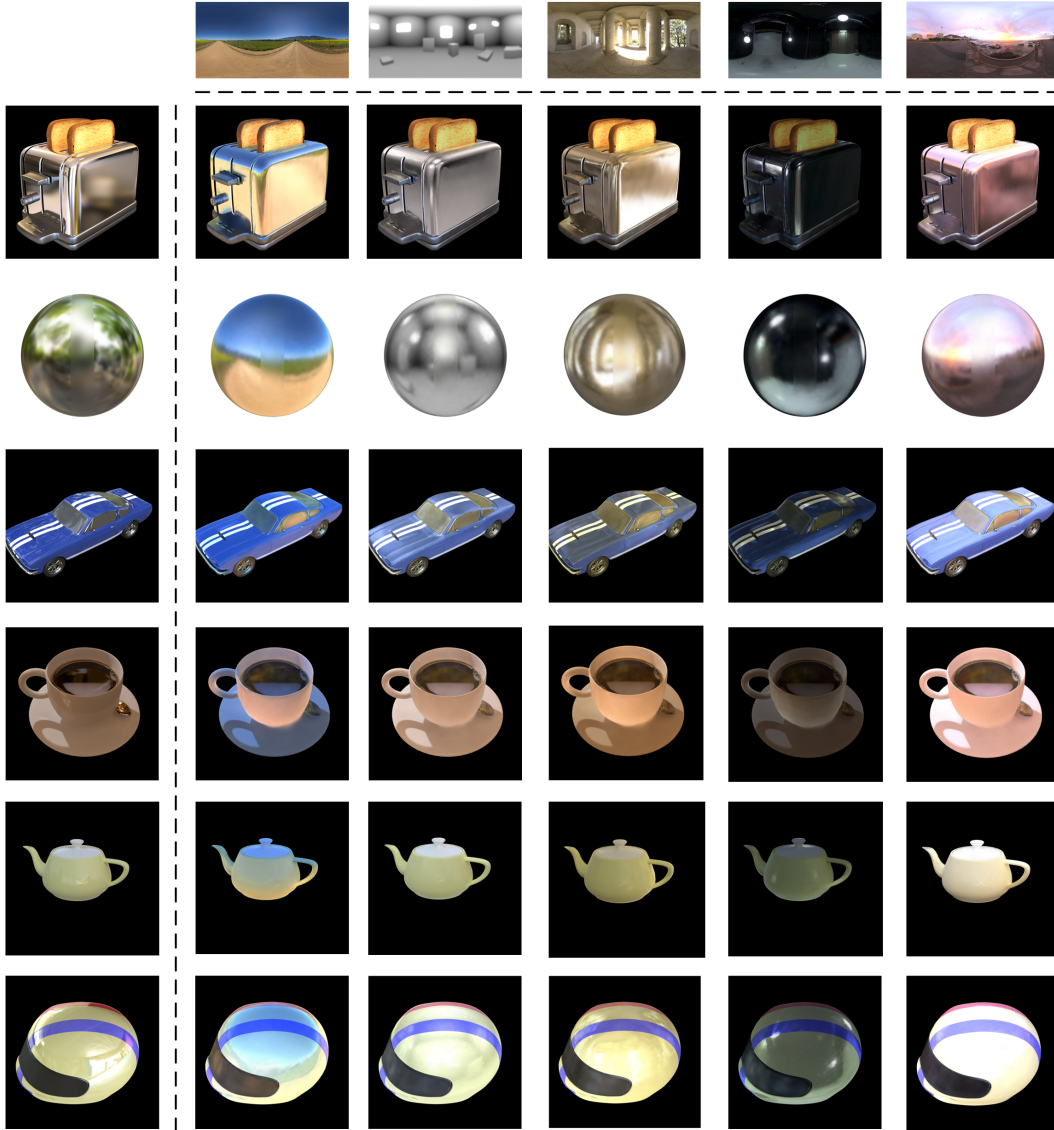


Figure 4. High quality relighting results achieved by our proposed method on Shiny Blender dataset [34].

Method	Novel View Synthesis					Relighting				
	Ficus	Hotdog	Lego	Armadillo	Avg.	Ficus	Hotdog	Lego	Armadillo	Avg.
NeRFactor [42]	21.664	26.479	26.076	26.479	25.175	20.684	22.713	23.246	26.887	23.383
InvRender [43]	22.131	31.832	24.391	31.116	27.368	20.330	27.630	20.117	27.814	23.973
NVDiffrec [25]	22.131	34.903	30.056	33.664	30.189	17.260	19.075	20.088	23.099	19.881
TensorIR [12]	29.780	36.820	34.700	39.050	35.088	24.296	27.927	28.581	34.504	28.827
Ours	37.352	37.916	36.269	43.379	38.792	31.927	23.331	24.261	27.472	26.748

Table 1. Quantative comparisons on TensorIR dataset. Our method exhibits strong performance (**PSNR**↑) in novel view synthesis and relighting tasks. The results show that our method can intrinsically factorize scene for high-quality rendering and relighting in real-time.

us to evaluate the quality of materials and rendering more accurately.

### 4.3. Benchmarking Results

**Relighting.** We perform relighting experiments on the TensorIR dataset, which includes three blender scenes from [23]



Figure 5. Qualitative evaluation of relighting on TensoIR dataset[12]. First row shows the HDR environment maps.

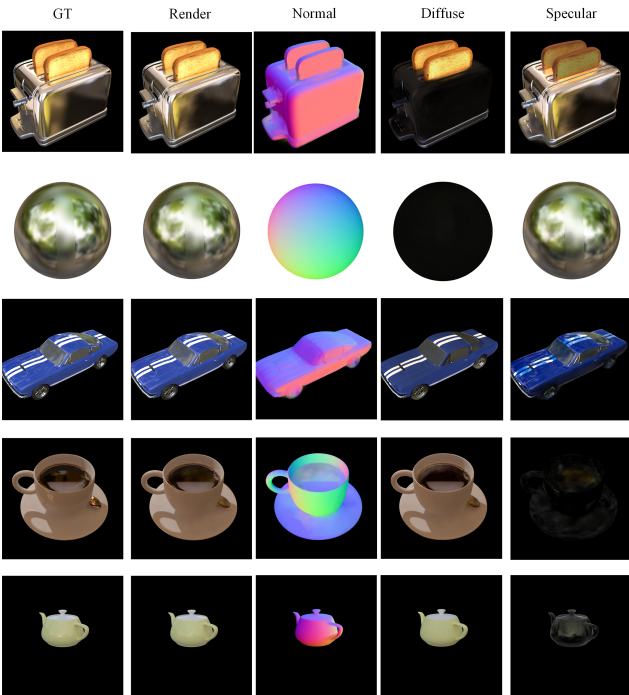


Figure 6. Qualitative evaluation of scene factorization on Shiny Blender dataset[34].

and an Armadillo model from Stanford 3D scanning repository [8]. This dataset includes rendered images with camera poses for reconstruction and ground truth under different HDR (5 in total) environments to evaluate relighting.

**Novel View Synthesis.** Novel view synthesis is a subtask of our work as a better performance on rendering novel views

Method	Car	Ball	Helmet	Teapot	Toaster	Coffee	Avg.
NVDiffRec[25]	27.98	21.77	26.97	40.44	24.31	30.74	28.70
NVDiffMC[10]	25.93	30.85	26.27	38.44	22.18	29.60	28.88
NeRO[18]	26.98	33.66	29.59	40.29	27.31	33.76	31.93
EnvIDR[17]	29.88	41.03	36.98	46.16	26.23	34.45	35.85
Ours	28.80	36.86	30.05	45.64	27.32	32.27	33.49

Table 2. The evaluation results of novel view synthesis (PSNR $\uparrow$ ) tested on Shiny Blender [34] dataset.

Method	Balloons	Hotdog	Chair	Jugs	Avg.
PhySG[41]	27.83	25.13	28.32	28.20	27.37
InvRender[17]	24.40	31.77	24.98	24.91	26.51
NVDiffrec[25]	29.90	33.68	29.16	25.30	29.51
Factored-NeuS[9]	33.89	36.71	34.58	36.48	35.41
Ours	37.74	38.49	39.56	42.57	39.59

Table 3. The evaluation results of novel view synthesis (PSNR $\uparrow$ ) tested on InvRender [43] dataset.

FCN	Geometry Reg.	Material Reg.	PSNR $\uparrow$
-	✓	✓	29.547
✓	-	-	32.638
✓	✓	-	32.465
✓	-	✓	33.026
✓	✓	✓	33.490

Table 4. The ablation study on evaluating the effectiveness of each proposed module and their combinations. FCN is the fully convolution layers for illumination (Sec. 3.3), geometry regulation, and material regulation (Sec. 3.2).

using physically-based rendering means a more plausible factorization of the underlying material properties and illumination. We evaluate the ability of novel view synthesis on the InvRender dataset, which is generated on 4 CAD models with obvious self-occlusion and multiple materials. Each of these is rendered using the natural environment. We also evaluate our method using the challenging Shiny blender dataset, which is first introduced in [34] and focuses on shiny materials with high-frequency reflections mixed with specular, glossy, and Lambertian materials. This includes six scenes in total, each containing 100 posed images from different viewpoints for training and 200 for evaluation. Our method exhibits strong performance against other inverse rendering approaches. We summarize the results in Tab. 2 and Tab. 3. Besides, we also provide additional qualitative results shown in Fig. 4, Fig. 7, Fig. 5 and 6, demonstrating the high-quality factorization and relighting achieved by our proposed methods.

#### 4.4. Ablation Study

We conducted an ablation study to verify each proposed module’s effectiveness and combinations. The results are presented in Tab. 4.



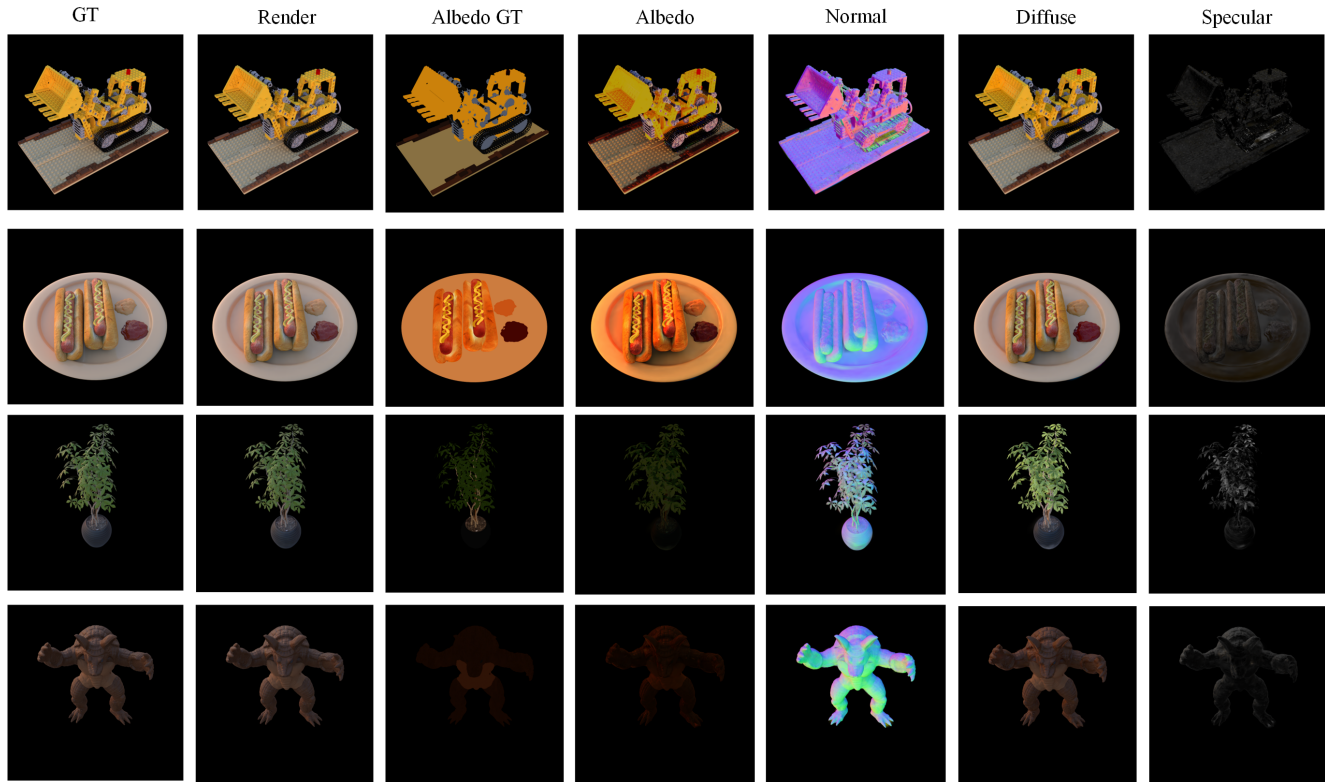


Figure 7. Qualitative results of scene factorization on TensoIR dataset[12].

## 5. Conclusion

This paper presents a 3D Gaussian-based inverse rendering method for relightable scene factorization. Our approach leverages the representation of Gaussian and the relationship between the normal and the smallest eigenvector of the covariance matrix. By simultaneously learning geometry, material properties, and illumination from multi-view image observations, our method enables various applications requiring material and environment interactions, such as relighting. Extensive experiments demonstrate the superior performance of our proposed method across multiple tasks in inverse rendering, highlighting its efficacy and broad applicability in relighting and scene reconstruction.

## References

- [1] Kara-Ali Aliev, Artem Sevastopolsky, Maria Kolos, Dmitry Ulyanov, and Victor Lempitsky. Neural point-based graphics. In *Computer Vision—ECCV 2020: 16th European Conference, Glasgow, UK, August 23–28, 2020, Proceedings, Part XXII 16*, pages 696–712. Springer, 2020. 2
- [2] Jonathan T Barron, Ben Mildenhall, Matthew Tancik, Peter Hedman, Ricardo Martin-Brualla, and Pratul P Srinivasan. Mip-nerf: A multiscale representation for anti-aliasing neural radiance fields. In *Proceedings of the IEEE/CVF International Conference on Computer Vision*, pages 5855–5864, 2021. 2
- [3] Jonathan T Barron, Ben Mildenhall, Dor Verbin, Pratul P Srinivasan, and Peter Hedman. Zip-nerf: Anti-aliased grid-based neural radiance fields. In *Int. Conf. Comput. Vis.*, 2023. 2
- [4] Mark Boss, Raphael Braun, Varun Jampani, Jonathan T. Barron, Ce Liu, and Hendrik P.A. Lensch. Nerf: Neural reflectance decomposition from image collections. In *Int. Conf. Comput. Vis.*, 2021. 3
- [5] Mark Boss, Varun Jampani, Raphael Braun, Ce Liu, Jonathan Barron, and Hendrik Lensch. Neural-pil: Neural pre-integrated lighting for reflectance decomposition. In *Adv. Neural Inform. Process. Syst.*, pages 10691–10704, 2021. 3
- [6] Brent Burley and Walt Disney Animation Studios. Physically-based shading at disney. In *Acm Siggraph*, pages 1–7. vol. 2012, 2012. 3
- [7] Charles Csuri, Ron Hackathorn, Richard Parent, Wayne Carlson, and Marc Howard. Towards an interactive high visual complexity animation system. *Acm Siggraph Computer Graphics*, 13(2):289–299, 1979. 2
- [8] Brian Curless and Marc Levoy. A volumetric method for building complex models from range images. In *Proceedings of the 23rd annual conference on Computer graphics and interactive techniques*, pages 303–312, 1996. 8
- [9] Yue Fan, Ivan Skorokhodov, Oleg Voynov, Savva Ignatyev,

- Evgeny Burnaev, Peter Wonka, and Yiqun Wang. Factored-neus: Reconstructing surfaces, illumination, and materials of possibly glossy objects. *arXiv preprint arXiv:2305.17929*, 2023. 3, 6, 8
- [10] Jon Hasselgren, Nikolai Hofmann, and Jacob Munkberg. Shape, Light, and Material Decomposition from Images using Monte Carlo Rendering and Denoising. In *Adv. Neural Inform. Process. Syst.*, 2022. 2, 3, 8
- [11] Jon Hasselgren, Nikolai Hofmann, and Jacob Munkberg. Shape, light, and material decomposition from images using monte carlo rendering and denoising. *Advances in Neural Information Processing Systems*, 35:22856–22869, 2022. 6
- [12] Haiyan Jin, Isabella Liu, Peijia Xu, Xiaoshuai Zhang, Songfang Han, Sai Bi, Xiaowei Zhou, Zexiang Xu, and Hao Su. Tensor: Tensorial inverse rendering. In *Proceedings of the IEEE/CVF Conference on Computer Vision and Pattern Recognition*, pages 165–174, 2023. 3, 6, 7, 8, 9
- [13] Brian Karis and Epic Games. Real shading in unreal engine 4. *Proc. Physically Based Shading Theory Practice*, 4(3):1, 2013. 4
- [14] Bernhard Kerbl, Georgios Kopanas, Thomas Leimkühler, and George Drettakis. 3d gaussian splatting for real-time radiance field rendering. *ACM Transactions on Graphics (ToG)*, 42(4):1–14, 2023. 2
- [15] Diederik P Kingma and Jimmy Ba. Adam: A method for stochastic optimization. *arXiv preprint arXiv:1412.6980*, 2014. 6
- [16] Marc Levoy and Turner Whitted. The use of points as a display primitive. 1985. 2
- [17] Ruofan Liang, Huiting Chen, Chunlin Li, Fan Chen, Selvakumar Panneer, and Nandita Vijaykumar. Envidr: Implicit differentiable renderer with neural environment lighting. In *Proceedings of the IEEE/CVF International Conference on Computer Vision*, 2023. 3, 6, 8
- [18] Yuan Liu, Peng Wang, Cheng Lin, Xiaoxiao Long, Jiepeng Wang, Lingjie Liu, Taku Komura, and Wenping Wang. Nero: Neural geometry and brdf reconstruction of reflective objects from multiview images. In *SIGGRAPH*, 2023. 2, 3, 4, 8
- [19] Jonathon Luiten, Georgios Kopanas, Bastian Leibe, and Deva Ramanan. Dynamic 3d gaussians: Tracking by persistent dynamic view synthesis. *arXiv preprint arXiv:2308.09713*, 2023. 2
- [20] Alexander Mai, Dor Verbin, Falko Kuester, and Sara Fridovich-Keil. Neural microfacet fields for inverse rendering. In *Proceedings of the IEEE/CVF International Conference on Computer Vision*, pages 408–418, 2023. 3
- [21] Shi Mao, Chenming Wu, Zhelun Shen, and Liangjun Zhang. Neus-pir: Learning relightable neural surface using pre-integrated rendering. *arXiv preprint arXiv:2306.07632*, 2023. 3, 4
- [22] Marko Mihajlovic, Silvan Weder, Marc Pollefeys, and Martin R Oswald. Deepsurfels: Learning online appearance fusion. In *Proceedings of the IEEE/CVF Conference on Computer Vision and Pattern Recognition*, pages 14524–14535, 2021. 2
- [23] Ben Mildenhall, Pratul P Srinivasan, Matthew Tancik, Jonathan T Barron, Ravi Ramamoorthi, and Ren Ng. Nerf: Representing scenes as neural radiance fields for view synthesis. *Communications of the ACM*, 65(1):99–106, 2021. 2, 7
- [24] Thomas Müller, Alex Evans, Christoph Schied, and Alexander Keller. Instant neural graphics primitives with a multiresolution hash encoding. *ACM Transactions on Graphics (ToG)*, 41(4):1–15, 2022. 2
- [25] Jacob Munkberg, Jon Hasselgren, Tianchang Shen, Jun Gao, Wenzheng Chen, Alex Evans, Thomas Müller, and Sanja Fidler. Extracting triangular 3d models, materials, and lighting from images. In *Proceedings of the IEEE/CVF Conference on Computer Vision and Pattern Recognition*, pages 8280–8290, 2022. 3, 4, 6, 7, 8
- [26] Fred E Nicodemus. Directional reflectance and emissivity of an opaque surface. *Applied optics*, 4(7):767–775, 1965. 1
- [27] Michael Oechsle, Songyou Peng, and Andreas Geiger. Unisurf: Unifying neural implicit surfaces and radiance fields for multi-view reconstruction. In *IEEE Conf. Comput. Vis. Pattern Recog.*, pages 5589–5599, 2021. 2
- [28] Ruslan Rakhimov, Andrei-Timotei Ardelean, Victor Lepitsky, and Evgeny Burnaev. Npbg++: Accelerating neural point-based graphics. In *Proceedings of the IEEE/CVF Conference on Computer Vision and Pattern Recognition*, pages 15969–15979, 2022. 2
- [29] Darius Rückert, Linus Franke, and Marc Stamminger. Adop: Approximate differentiable one-pixel point rendering. *ACM Transactions on Graphics (ToG)*, 41(4):1–14, 2022. 2
- [30] Christophe Schlick. An inexpensive brdf model for physically-based rendering. In *Computer graphics forum*, pages 233–246. Wiley Online Library, 1994. 4
- [31] Tianchang Shen, Jun Gao, Kangxue Yin, Ming-Yu Liu, and Sanja Fidler. Deep marching tetrahedra: a hybrid representation for high-resolution 3d shape synthesis. *Advances in Neural Information Processing Systems*, 34:6087–6101, 2021. 3
- [32] Pratul P Srinivasan, Boyang Deng, Xiuming Zhang, Matthew Tancik, Ben Mildenhall, and Jonathan T Barron. Nerv: Neural reflectance and visibility fields for relighting and view synthesis. In *IEEE Conf. Comput. Vis. Pattern Recog.*, pages 7495–7504, 2021. 3
- [33] Jiayang Tang, Jiawei Ren, Hang Zhou, Ziwei Liu, and Gang Zeng. Dreamgaussian: Generative gaussian splatting for efficient 3d content creation. *arXiv preprint arXiv:2309.16653*, 2023. 2
- [34] Dor Verbin, Peter Hedman, Ben Mildenhall, Todd Zickler, Jonathan T Barron, and Pratul P Srinivasan. Ref-nerf: Structured view-dependent appearance for neural radiance fields. In *IEEE Conf. Comput. Vis. Pattern Recog.*, pages 5481–5490. IEEE, 2022. 2, 3, 7, 8
- [35] Bruce Walter, Stephen R Marschner, Hongsong Li, and Kenneth E Torrance. Microfacet models for refraction through rough surfaces. In *Proceedings of the 18th Eurographics conference on Rendering Techniques*, pages 195–206, 2007. 3
- [36] Peng Wang, Lingjie Liu, Yuan Liu, Christian Theobalt, Taku Komura, and Wenping Wang. Neus: Learning neural implicit surfaces by volume rendering for multi-view reconstruction. In *Adv. Neural Inform. Process. Syst.*, 2021. 2

- [37] Qiangeng Xu, Zexiang Xu, Julien Philip, Sai Bi, Zhixin Shu, Kalyan Sunkavalli, and Ulrich Neumann. Point-nerf: Point-based neural radiance fields. In *Proceedings of the IEEE/CVF Conference on Computer Vision and Pattern Recognition*, pages 5438–5448, 2022. 2
- [38] Yao Yao, Jingyang Zhang, Jingbo Liu, Yihang Qu, Tian Fang, David McKinnon, Yanghai Tsin, and Long Quan. Neif: Neural incident light field for physically-based material estimation. In *Eur. Conf. Comput. Vis.*, pages 700–716. Springer, 2022. 3, 6
- [39] Lior Yariv, Jiatao Gu, Yoni Kasten, and Yaron Lipman. Volume rendering of neural implicit surfaces. *Advances in Neural Information Processing Systems*, 34:4805–4815, 2021. 2
- [40] Jingyang Zhang, Yao Yao, Shiwei Li, Jingbo Liu, Tian Fang, David McKinnon, Yanghai Tsin, and Long Quan. Neif++: Inter-reflectable light fields for geometry and material estimation. In *Proceedings of the IEEE/CVF International Conference on Computer Vision*, 2023. 3
- [41] Kai Zhang, Fujun Luan, Qianqian Wang, Kavita Bala, and Noah Snavely. Physg: Inverse rendering with spherical gaussians for physics-based material editing and relighting. In *IEEE Conf. Comput. Vis. Pattern Recog.*, pages 5453–5462, 2021. 3, 8
- [42] Xiuming Zhang, Pratul P Srinivasan, Boyang Deng, Paul Debevec, William T Freeman, and Jonathan T Barron. Nerfactor: Neural factorization of shape and reflectance under an unknown illumination. *ACM Trans. Graph.*, 40(6):1–18, 2021. 3, 6, 7
- [43] Yuanqing Zhang, Jiaming Sun, Xingyi He, Huan Fu, Rongfei Jia, and Xiaowei Zhou. Modeling indirect illumination for inverse rendering. In *CVPR*, 2022. 7, 8
- [44] Yuanqing Zhang, Jiaming Sun, Xingyi He, Huan Fu, Rongfei Jia, and Xiaowei Zhou. Modeling indirect illumination for inverse rendering. In *Proceedings of the IEEE/CVF Conference on Computer Vision and Pattern Recognition*, pages 18643–18652, 2022. 6